



NLR-TP-2014-504

A discussion of measured static and dynamic rotor loads during testing of the ERICA tilt-wing rotorcraft configuration in DNW-LLF wind tunnel

A.C. de Bruin and O. Schneider

Nationaal Lucht- en Ruimtevaartlaboratorium

National Aerospace Laboratory NLR

Anthony Fokkerweg 2

P.O. Box 90502

1006 BM Amsterdam

The Netherlands

Telephone +31 (0)88 511 31 13

Fax +31 (0)88 511 32 10

www.nlr.nl



Executive summary

A discussion of measured static and dynamic rotor loads during testing of the ERICA tilt-wing rotorcraft configuration in DNW-LLF wind tunnel



Report no.

NLR-TP-2014-504

Author(s)

A.C. de Bruin
O. Schneider

Report classification

UNCLASSIFIED

Date

November 2014

Knowledge area(s)

Helikoptertechnologie
Aëro-akoestisch en experimenteel
aërodynamisch onderzoek

Descriptor(s)

Wind Tunnel Tests
Tilt Rotor Aircraft

Problem area

As part of the EU NICETRIP research project a heavily instrumented model of the ERICA tilt wing configuration was tested in the DNW-LLF low speed wind tunnel. The outer wing and the rotor of the ERICA configuration can be tilted independently, which offers many advantages during the transition from hover to forward flight, compared to a configuration where only the rotor can be tilted. Also during the high thrust hover stage, the rotor efficiency is significantly improved when the outer wing is tilted and does not

block the downwash of the rotor. This enables the use of a smaller rotor diameter and therefore the ERICA configuration can also take-off and land as a normal airplane. Tests in DNW-LLF ranged from pure helicopter and conversion corridor cases up to a low speed aircraft mode. In total over 400 test conditions were measured. The main purpose of the test was to create a database for the time-mean aerodynamic forces and moments on the model, to be used for the validation of the flight mechanics model of the tilt-wing configuration.

This report is based on a presentation held at the European Rotorcraft Forum, Southampton, September 2-5, 2014.

Besides the steady forces, also unsteady (cyclic) rotor induced forces and moments and unsteady pressures and nacelle vibration levels were measured.

Challenges during the tests

The actual ERICA concept will use gimballed rotors. However, due to size limitations these could not be realized in the 1:5 scale wind tunnel model. Instead, cyclic blade pitch control through a swash plate was applied in the model. Cyclic and collective blade pitch settings are remote controlled, such as to allow pilot controlled adjustments for model trimming (thrust) and for minimum rotor in-plane forces and moments, as occurring with a gimbal solution. However, during testing it appeared that the rotor blade pitch bearings were too heavily loaded, which led to their ultimate failure. Therefore the majority of tests had to be done without cyclic pitch. This in turn caused quite high bending moments in the rotor axis, which had to be carefully monitored. Some test conditions were both investigated with- and without cyclic blade pitch control. The high unsteady loads experienced during the tests and the high vibration levels observed occasionally, motivated the present analysis of unsteady forces.

Description of work

The present report does focus on the steady and unsteady rotor loads and also related nacelle vibration levels were investigated. The analysis of the steady aerodynamic loads on the model has been made elsewhere in the NICETRIP project.

Results and conclusions

It is found that with cyclic blade pitch control the time mean rotor in-plane forces and moments and the 1/rev rotor shaft and blade bending moments are effectively suppressed, but the dynamic components of the rotor in-plane forces and moments become larger than without cyclic blade pitch control.

Applicability

The measured data are well suited to validate or verify existing semi-empirical or CFD methods to predict the steady and unsteady loads of the rotors in close proximity to the wing leading edge. It should however be noted that the majority of the presented results are not directly transferable to the full scale ERICA concept, because ERICA will use gimballed rotors, whereas the majority of the DNW-LLF tests was done without cyclic blade pitch. Also, vibration characteristics of the wind tunnel model are expected to be different from that of the full scale ERICA concept.



NLR-TP-2014-504

A discussion of measured static and dynamic rotor loads during testing of the ERICA tilt-wing rotorcraft configuration in DNW-LLF wind tunnel

A.C. de Bruin and O. Schneider¹

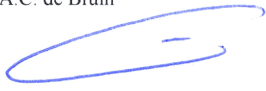
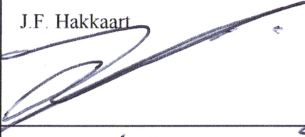

¹ DLR

This report is based on a presentation held at the European Rotorcraft Forum, Southampton, September 2-5, 2014.

The contents of this report may be cited on condition that full credit is given to NLR and the authors.
This publication has been refereed by the Advisory Committee AEROSPACE VEHICLES.

Customer European Commission
Contract number - - -
Owner NLR + partner(s)
Division NLR Aerospace Vehicles
Distribution Unlimited
Classification of title Unclassified
Date November 2014

Approved by:

Author A.C. de Bruin 	Reviewer J.F. Hakkaart 	Managing department J.F. Hakkaart 
Date: 5/1/2015	Date: 5/1/2015	Date: 5/1/2015



Contents

Abstract	3
Introduction	3
Model, instrumentation and test matrix	3
The rotors and their operation	4
Rotor load measurements	5
Model operation and trimming	6
Comparison of trimmed test cases without cyclic pitch	6
Possible cause of the 2/rev blade bending mode	7
The loads on the rotor shaft bearings	8
Concluding remarks	8
COPYRIGHT STATEMENT	8

A DISCUSSION OF MEASURED STATIC AND DYNAMIC ROTOR LOADS DURING TESTING OF THE ERICA TILT-WING ROTORCRAFT CONFIGURATION IN DNW-LLF WIND TUNNEL

Anton de Bruin (anton.de.bruin@nlr.nl, NLR, Voorsterweg 31, 8316PR Marknesse, the Netherlands),
Oliver Schneider (oliver.schneider@dlr.de, DLR, Lilienthalplatz 7, 38108 Braunschweig, Germany)

Abstract

A heavily instrumented 1:5 scaled model of the ERICA tilt-wing configuration has been tested in the DNW-LLF wind tunnel as part of the EU co-funded NICETRIP project. Tests were made for a variety of conditions ranging from pure helicopter and conversion corridor cases up to a low speed aircraft mode, with appropriate changes in tilt rotor and outer wing pitching angles. In total over 400 test conditions were measured. Rotor forces and moments have been measured with rotor balances. Blade bending moment and torsion as well as rotor shaft bending and torque were measured with calibrated strain gauge sensors. Measurements were made for fully trimmed and for non-trimmed conditions. The four bladed rotors are counter-rotating, are rigid in plane and allow cyclic blade pitch control through a remote controlled swash plate. Since cyclic pitch control caused damage to the blade pitch bearings, most of the test conditions had to be done without cyclic blade pitch control, leading to a large in-plane moment in the rotor plane and high bending moments in the rotor shaft. Some test cases were both measured with and without cyclic pitch control.

The present paper analysis the rotor induced forces, moments and nacelle vibrations for the trimmed conditions. Both steady and dynamic contents of the signals are analyzed. It is found that with cyclic blade pitch control the time mean rotor in-plane forces and moments and the 1/rev rotor shaft and blade bending moments are effectively suppressed, but the dynamic components of the rotor in-plane forces and moments become larger than without cyclic blade pitch control. Without cyclic blade pitch control the 1/rev blade and rotor shaft bending moments become quite large and, rather surprisingly, for some of these test conditions also a large 2/rev blade bending moment is observed. Careful analysis of the data suggests that the 2/rev flap bending is caused by a 1/rev excitation (in the non-rotating system) of both nacelles, caused by the proximity of the nominal rotor rpm frequency to symmetric and anti-symmetric nacelle torsion eigenfrequency and probably also in combination with other nacelle related eigen-modes.

The measured data are well suited to validate or verify existing semi-empirical or CFD methods to predict the steady and unsteady loads of the rotors. A correlation between rotor dynamics and (outer) wing dynamic loading and the influence of the outer wing and/or flaperon setting on the rotor forces and moments is left for future analysis.

Introduction

As part of the EU co-funded 6th Framework NICETRIP project, a 1:5 scale model of the ERICA tilt-wing configuration was tested in the 9.5x9.5 m² test section of the low speed DNW-LLF wind tunnel in June 2013. These tests were made in the low velocity regime until $Ma=0.17$ ($V=59$ m/s). In May 2014 also high speed tests up to $Ma=0.55$ have been performed in ONERA-S1 wind tunnel. Prior to the tests ground vibration tests of the model were made by DLR Goettingen in order to assure a safe operation of the model. The model design and manufacturing was largely done by NLR, with inputs from TsAGI (outer geometry shells) and ONERA (rotor balances and blade design). The overall project was led by Agusta Westland. The present paper only deals with the low speed DNW-LLF tests and focus is on the rotor loads.

Model, instrumentation and test matrix

The model has a wing span of 3 m and two 1.48 m diameter rotors placed at the wing tips. Both rotors are operated at the same rotational speed (rpm) by a central gearbox, driven by two air motors. The pitch angle of the outer wing and that of the nacelles can be changed independently, but the nacelle pitch angle needs to remain larger than that of the outer wing. A sketch showing the remote controlled movable surfaces of the model is shown in Figure 1 and model dimensions are shown in Figure 2.

The test matrix in the DNW-LLF wind tunnel included 7 trimmed conditions in helicopter (3x), conversion (3x) & aircraft mode (1x). An overview of the trimmed conditions tested is given in Table 1. For these tests the total lift of the model is trimmed to the scaled down full aircraft design weight and the total drag and pitching moment are trimmed to zero.

All test conditions in DNW-LLF apply to zero altitude flight conditions. In helicopter mode the trimming is mainly done by adjusting blade collective pitch and thus rotor thrust. In aircraft mode lift is mainly controlled by aircraft pitching angle and drag by blade collective pitch control. Depending on test condition, the nacelle pitching angle varies between 0 deg (AC1 aircraft mode) and about 90 deg (HC1 pure helicopter mode). For the trimmed conditions, a visual display of the rotor position with respect to the wing (blue lines) and with respect to the fuselage center line (red dashed line) is shown in Figure 3. The average thrust and F_z force vectors are indicated by red lines, showing that max thrust is needed in helicopter mode and minimum thrust is needed in aircraft mode. A significant in-plane force component F_x is only observed for the CC4 case. Here $_cy$ denotes a test case with and $_nc$ a test case without cyclic pitch control. Figure 4 shows the different (trimmed) test conditions in the wind tunnel velocity and nacelle pitch angle space.

The model is mounted on an internal 6-component main balance on the dorsal sting support in DNW-LLF (see Figure 5). This allows the Load Reference Point (LRP) of the model to be kept at the test section center line, while performing alpha and beta changes in model attitude.

For each case a comprehensive number of variations (*model incidence or sideslip, nacelle tilting angle, outboard wings tilting angle, flap, flaperons, rudder and elevator deflection angles and blade collective pitch angles*) were performed in order to provide data for the flight dynamic model data-base. In total, over 400 different flight conditions, including an exploration towards the boundary of the conversion corridor, were measured.

The model was heavily instrumented. Model trimming and quick model changes were enabled by a model-pilot interface from DLR to operate 16 (!) remote controls for cyclic pitch of the rotor blades (6x), rudder (1x), elevator (1x), outer wings (2x), nacelles (2x), flaperons (2x) and flaps (2x). The model-pilot interface is shown in Figure 6. Total forces, rotor and tail forces were measured with 6-component balances. Flaperon, flap, rudder and elevator moments were dynamically measured with one-component local balances. In addition various local loads and temperatures were dynamically measured and monitored for safety reasons. This included measurement of blade bending and torsion moments (1 blade/rotor), rotor shaft bending moments, rotor shaft torque (independent of rotor balance torque), swash plate actuator forces (2/rotor) and various accelerometer signals. For each flight condition, over 800 parameters were recorded; including about 50 parameters from balance loads, strain gauges and accelerometers,

flight control positions, required power and 678 static (mainly at Left Hand (LH) side of model) and 55 dynamic pressures (only at Right Hand (RH) side of the model). All dynamic sensor signals, including rotor loads, were evaluated and stored up to the 8th harmonic in amplitude and phase, using a harmonic analysis of the signals from 32 rotor revolutions. The tests resulted in an extensive and valuable database for the validation of the ERICA tilt-wing/tilt-rotor concept.

Due to the complexity of the model and the numerous aircraft design variables to be measured, testing was extremely challenging and many minor and larger issues were encountered and needed to be solved during the tests. Nevertheless, the test was successfully completed, thanks to the skill and experience of the integrated Agusta Westland, DNW, DLR and NLR teams.

The rotors and their operation

The rotors of the ERICA configuration are relatively large in order to provide sufficient thrust for a vertical take-off and landing. However the aircraft may also take-off and land as a normal airplane. The rotors, designed by ONERA and Agusta Westland, are situated at the tip of the wing and at a relatively short distance from the $\frac{1}{4}$ chord line (≈ 0.5 rotor radius). Combined with the fact that unusual large pitch angles of the rotors occur, this requires them to operate in a very non-uniform flow field under most of the testing conditions. The nominal rotations per minute (rpm) of the rotor in all non-aircraft modes is 2765 ($Ma_{tip}=0.630$) and in aircraft mode it is 2130 ($Ma_{tip}=0.485$). The actual rpm during the wind tunnel test is adapted depending on the static temperature in the wind tunnel. For the AC1 and CC4 test conditions the requested wind tunnel Mach number could not be reached (reduced to 98%), which required a small reduction in rpm to keep the design advance ratio μ .

The ERICA full scale configuration will use gimballed rotors. However, these could not be implemented in the relatively small wind tunnel model. Instead the blades are stiff in plane (both in blade flapping and in lead/lag motion) and a swash plate operated cyclic blade pitch control was implemented to keep the rotor in-plane moments close to zero during all test conditions. The collective and cyclic pitch of the blades of each rotor is operated through three remotely controlled actuators for setting the position of the swash plate. This allows adjustment of the thrust (collective pitch changes) for overall model trimming and trimming to near-zero rotor in-plane moments.

Figure 7 shows the blade shaft mounting to the rotor hub. Blade aerodynamic loading is mainly normal to the blade chord, causing a time-varying force and a bending moment to the blade shaft. These mainly result in forces on bearings #1 and #2. The centrifugal load leads to a large axial force along the blade shaft (about 12kN at 2100 rpm and about 20kN at 2730 rpm), which is mainly taken by axial bearing #3. Since this axial bearing is tightly mounted, the (unsteady) blade shaft bending loads are not only taken by bearings #1 and #2 but also partially by axial bearing #3. Without cyclic blade pitch control there is no blade pitch movement. With cyclic blade pitch control the axial bearing is heavily loaded under rapid (about 46 /s) back and forth blade pitching movement. With 20 cylinder type bearings around the circumference, and small but rapid pitch angle movements, the cylinders have only a limited rolling motion. Therefore the lubrication is not ideal and with high loading this leads to high friction and local heating problems. Indeed, after having tested conditions AC1 and CC4 (partly) in cyclic pitch control mode, unexpected damage to the blade axis bearings was encountered (see Figure 8). After repair, tests were continued with HC2 but caused again damage. Therefore, all remaining tests were made without cyclic pitch control.

However, with a relatively high pitch attitude of the rotor axis, combined with relatively high tunnel speeds during part of the tests and a non-uniform flow field in the rotor plane caused by the wing, a high dynamic load on the blades, the rotor axis and the rotor balances occurred. These had to be carefully monitored for a safe operation of the model and it ultimately required a 10% reduction in the wind tunnel speed for the HC3 and CC2 test conditions.

Rotor load measurements

Each rotor balance consists of a fixed balance part measuring the in-plane forces and moments and the rotor thrust and a rotating part measuring the rotor torque. A sketch is shown in Figure 9, showing the rotor shaft bearing house mounted on the fixed part of the rotor balance and fixed balance adapter (respectively in blue and brown) and the rotor shaft mounted on the rotating part of the rotor balance (in red). Note that the right hand side of the figure does not represent the actual situation in which the rotating balance is mounted to a drive shaft. The rotor balance has been carefully calibrated under static conditions. Calibrations showed the max error to be less than 0.5% of max calibration range for the rotor thrust (3140 N) and torque (466 Nm). Larger but acceptable max errors occur for the in-plane

moments (error < 20 Nm) and forces (error < 40 N). The origin of the rotor coordinate system is at the rotor plane center, as shown in Figure 10. Figure 11 displays the relationship between the rotor force F_z , the rotor moment M_y and the vertical forces on the rotor shaft bearings, indicated as $F_{z,b1}$ and $F_{z,b2}$, located at 73.5 and 177.5 mm downstream of the rotor plane.

Mainly for safety monitoring, the rotor shaft bending and torsion moments, blade bending and torsion moments, blade pitch arm bending moments and swash plate actuator rod loads are measured with calibrated strain gauge bridges. The rotor shaft bending and torsion moments are measured with strain gauges at about 40 mm downstream of the rotor plane (see figure 11). The following relations apply for force and moment equilibrium of the rotor shaft:

$$(1) \quad F_{z,b1} + F_{z,b2} + F_z = 0$$

$$(2) \quad M_y - F_z * 0.0735 + F_{z,b2} * 0.104 = 0$$

From which follows:

$$(3) \quad F_{z,b2} = (F_z * 0.0735 - M_y) / 0.104$$

$$(4) \quad F_{z,b1} = -(F_z * 0.1775 - M_y) / 0.104$$

From measured F_z and M_y the shaft bending moment at the position of the strain gauge can be computed from:

$$(5) \quad M_{y,shaft} = M_y - 0.040 * F_z$$

In the above, sub-fix b1 and b2 denote bearing #1 and #2 of the rotor shaft. Similar relations are found for the other force and moment components:

$$(6) \quad F_{y,b2} = (F_y * 0.0735 + M_z) / 0.104$$

$$(7) \quad F_{y,b1} = -(F_y * 0.1775 + M_z) / 0.104$$

$$(8) \quad M_{z,shaft} = M_z + 0.040 * F_y$$

The total shaft bending moment and the total bearing force can be computed by appropriate summing of both components. E.g. the total shaft bending moment follows from:

$$(9) \quad M_{shaft} = \sqrt{M_{y,shaft}^2 + M_{z,shaft}^2}$$

To monitor the vibration levels a 3-axis accelerometer is installed on each nacelle, its position is shown in figure 12. Signals from the

rotating parts are measured through a slip-ring. Since some of the slip-ring signals of the left-hand rotor were missing during part of the tests, the present data analysis is focused on the right-hand (RH) rotor. If the n/rev acceleration amplitude is equal to A_n , the corresponding displacement amplitude D_n is:

$$(10) \quad D_n = A_n / (2\pi n * \text{rpm}/60)^2$$

Phase averaged time signals can be reconstructed from the 1 to 8/rev recorded measurement data. E.g. for signal V , having V_0 as time mean value and V_n and ψ_n as n/rev amplitude and phase angle:

(11) Error! Objects cannot be created from editing field codes.

A summary of the steady and unsteady forces and moments related to the rotor is presented below.

Model operation and trimming

Trimming of the model was done aiming for zero total forces and moments (corrected for model weight) at the load reference point (LRP), where the center of gravity is assumed to be. Thus the model was in trimmed condition when the total drag and side force were equal to zero, and rolling, pitching and yawing moment of the total model were equal to zero. The total lift of the model is trimmed to the scaled down full aircraft design weight ($m=10000$ kg), taking account of the static pressure difference between tunnel and real flight: $L = mgE^2(\rho_{\text{tunnel}}/\rho_{\text{flight}})$, where $E=0.2$ is the model scale factor.

When cyclic blade pitch control was used, prior to final trimming both rotors were trimmed to zero in-plane moments to mimic a gimbaled rotor where no moments do occur. This was done by adjusting the 1/rev shaft bending to zero.

Effect of cyclic pitch control on rotor loads

For HC2 and CC4 a comparison between the load levels of the cyclic ($_cy$) and no-cyclic ($_nc$) trimmed conditions (see table 1) can be made. Figure 13 shows the blade pitch angle as function of blade #1 position (as defined in Figure 10: $\psi=0$ with blade #1 in top position). The amplitude for the blade pitch angle movement is 5.44 deg for CC4 and 6.26 deg for HC2.

Figure 14 shows the static and the 1 until 8 per revolution (1-8/rev) blade bending moment (+ for blade up) of blade #3 (the blue blade in Figure 10). For the HC2 configuration the static blade bending moment is much larger because of the higher thrust level (HC2: 1630 N, CC4: 430 N). It can be observed that without cyclic pitch control there is a very large

1/rev variation in blade bending amplitude. There is also a quite large 2/rev amplitude, especially when there is cyclic blade pitch control. Figure 15 shows the reconstructed time signals for the blade bending moment. The variation in blade bending moment during one blade revolution is quite large, especially without cyclic pitch control, where the blade bending moment even changes sign.

Figure 16 shows that without cyclic blade pitch control the 1/rev rotor shaft bending moment becomes quite large. With cyclic pitch control, which is 1/rev by definition, the 1/rev blade bending and the rotor shaft bending moments become much lower. With cyclic pitch the mean static rotor in-plane moments M_y and M_z are effectively trimmed to a lower value (see Figures 17 and 18), but it can be observed that the 4/rev and 8/rev in-plane moment components become higher with cyclic pitch control. This is also observed for the in-plane forces F_y and F_z (see Figures 19 and 20). The 4/rev (and 8/rev) components of rotor in-plane forces and moments lead to a substantial increase of the 4/rev nacelle vibration in rotor coordinate z-direction (see Figure 21). From equation 10 it follows that for a 70 m/s² amplitude of the 4/rev acceleration the corresponding displacement amplitude is only 0.05 mm.

Reconstructed time signals for M_z , F_z and nacelle z-acceleration signals (see figure 12 for accelerometer position) are shown in Figures 22-24.

Figure 25 shows that there is a good agreement between the measured time averaged total rotor in-plane moment, the computed time averaged rotor shaft bending moment at the strain gauge position and the strain gauge measured 1/rev rotor shaft bending moment. With reference to equation 5 and 8 it must be concluded that the contribution of the in-plane rotor forces to the rotor shaft bending moment is relatively small.

Comparison of trimmed test cases without cyclic pitch

Now focus is on the test cases without cyclic pitch control, but the AC1 case, having only small cyclic pitch, is included for completeness. The test conditions differ in effective rotor pitch angle, forward speed, collective blade pitch angle setting and pitch angle setting of the outer wing. HC1 test condition is at zero forward speed, HC2 is at 20 m/s and HC3 is at 36 m/s (see Table 1). In helicopter mode the rotor tilt angle with respect to the flow direction (tunnel axis) changes from 89.9 to 81.5 deg, while the outer wing pitch angle changes from 80 to 18.6 deg (see Table 1 and Figures 3 and 4).

For CC1 the rotor tilt angle with respect to tunnel axis is nearly the same than for HC3, but the velocity is lower (30.3 m/s) and the wing and nacelle angle are different (see Figure 4 and Table 1). The rotor tilt angle and forward speed are 64.2 deg and 49.3 m/s for CC2, 35.3 deg and 59.1 m/s for CC4 and 10 deg and 59.1 m/s for AC1. It should be noted that a 10% reduced rotor rpm has been used for HC3 and CC2 (see Table 1). For the different test cases the rotor thrust and direct installed lift (taking into account the contribution of the thrust and the rotor in-plane force F_z) is shown in Figure 26. Data have been ordered in sequence of forward speed magnitude. The red broken line represents the required total lift for trimming (per model side, so half of the total lift required for the 1:5 scaled model), showing that for the HC1 mode the complete lift has to come from the rotor, whereas for AC1 mode almost all lift needs to be created by the wing. Figure 27 shows the collective blade pitch angle for the trimmed conditions.

Figure 28 shows mean and n/rev components of the blade bending moment. Figure 29 and 30 show the corresponding reconstructed time signals for the HC and CC flight conditions, confirming a relatively large amplitude of the $2/\text{rev}$ component for the CC1 but especially for the HC3 and CC2 conditions. Figure 31 shows the mean and n/rev components of the measured rotor shaft bending moment. It is dominated by the $1/\text{rev}$ component, caused by the fact that without cyclic blade pitch the in-plane rotor moments are relatively large. Figure 32 and 33 show the mean and n/rev components for the rotor in-plane moments M_y and M_z and Figure 34 and 35 show the in-plane forces F_y and F_z . It can be observed that the in-plane rotor forces mainly have $1/\text{rev}$, $4/\text{rev}$ and $8/\text{rev}$ content. However, occasionally other modes seem active too, e.g. the $3/\text{rev}$ mode in the HC3 and CC2 case.

Figure 36 shows that there is a good comparison between the measured time mean total rotor in-plane moment (the square root sum of the measured M_y and M_z components), the computed time mean rotor shaft bending moment at strain gauge position (from equation 9) and the $1/\text{rev}$ rotor shaft bending moment measured with the strain gauge. Again the in-plane forces have only a small contribution to the shaft bending moments, as computed from equation 5 and 8. Figure 37 compares the measured torque from the rotor balance with the measured torque from the rotor shaft strain gauge torque sensor. Although the rotor shaft strain gauge sensor was only meant for monitoring, it appears that in most cases there is a rather good agreement with the rotor balance derived data.

Figure 38 shows that the z -component of the nacelle acceleration is quite high for all HC cases and for the CC1 case. It should be noted that the z -acceleration is measured at an aft position in the nacelle. The unsteady rotor force F_z and rotor in-plane moment M_y are the main driving forces causing both pure z -translations and pitching movements of the nacelle. If the amplitude of the n/rev mode acceleration has amplitude A_n , the corresponding displacement has amplitude $|B| = A_n / (n\omega)^2$, with $\omega = 2\pi f = 2\pi n (\text{rpm}/60)$. This shows that for a given acceleration amplitude and rotor rpm the displacement amplitude rapidly decreases with n . A $1/\text{rev}$ acceleration amplitude of $1g$ corresponds to a displacement amplitude of less than 0.2 mm.

Possible cause of the $2/\text{rev}$ blade bending mode

The large $2/\text{rev}$ blade bending moments, for some of the test conditions, needs some further analysis. Suppose that the nacelle displays a $1/\text{rev}$ rotation around the wing axis (quarter chord line). A $1/\text{rev}$ pitching mode of the rotor axis will induce a $2/\text{rev}$ motion in the rotating system. E.g. suppose that the blade is in upright position while there is a pitch-up motion of the rotor axis. Then a pitch down motion of the rotor axis will occur when the blade is in downward position. Thus at both positions of the blade, the blade is pushed backwards, showing that a $1/\text{rev}$ pitching of the rotor axis creates a $2/\text{rev}$ motion of the blade in the rotating frame. Indirect evidence for such a pitching motion of the rotor axis can be found in the $1/\text{rev}$ z -acceleration signals for the LH and RH nacelle, e.g. as shown in figure 39 for the CC1 case. In this case a phase shift between both signals of about 180 deg is observed, which means that the vibration of LH and RH nacelle is anti-symmetric. During ground vibration tests indeed an anti-symmetric nacelle pitch motion Eigen-mode has been detected with different frequencies for the AC (38.74 Hz) and HC condition (47.77 Hz, decreasing with up to 4 Hz at increased force levels). A symmetric nacelle pitch motion Eigen-mode could be found at 42.6 Hz in AC mode and 44.8 Hz in HC mode. Both Eigen-mode frequencies are quite close to the $1/\text{rev}$ of the AC and HC condition. Also some other nacelle related Eigen-modes, found during the ground vibration tests, are quite close to the nominal rotor rpm. The blade bending moments of the counter-rotating LH and RH rotor are compared in figure 40 for the CC1 condition, showing that both are nearly identical, also in the $2/\text{rev}$ phase. It is concluded that the strong $2/\text{rev}$ blade bending is most likely caused by a $1/\text{rev}$ excitation of the nacelle by some remaining unbalance in the rotor systems. This is obviously caused by the proximity of the rotor rpm frequency to the symmetric and anti-

symmetric nacelle torsion Eigen-frequency, probably in combination with other nacelle related Eigen-modes.

The loads on the rotor shaft bearings

For the HC2 and CC4 configuration with and without cyclic pitch, the computed rotor shaft bearing #1 force components $F_{y,b1}$ and $F_{z,b1}$ (see figure 11 for definition) during one rotor shaft revolution are shown in figure 41. Without cyclic pitch control the rotor in-plane moments are relatively large and cause quite large loading of the rotor shaft. Therefore without cyclic pitch the forces on the bearing become quite large, but the variation in force is less than for the cases with cyclic pitch control.

Similarly, results for the HC1, HC2 and HC3 configurations are shown in figure 42, and for the CC1, CC2 and CC4 configurations in figure 43. These results are for the case without cyclic pitch and thus result in quite high forces, especially for configuration CC1.

Concluding remarks

The tests with the highly instrumented wind tunnel model provided a large volume of data for each test point. In the present study only a small part of that data has been evaluated, since focus was on the rotor induced forces and moments for trimmed conditions only. Both time mean and unsteady forces and moments were analyzed.

Since the tests in DNW-LLF focused on the low speed conditions in helicopter mode and on test conditions in the conversion corridor up to a low speed aircraft mode, the rotor operated under a large range of thrust and pitch angle conditions.

Tests started with cyclic blade pitch control for AC1, HC2 and CC4 to minimize the in-plane rotor moments. However this led to damaged axial blade shaft bearings. Therefore the remaining tests were made without cyclic blade pitch control.

However, this caused relatively large 1/rev bending moments in the rotor shafts which had to be closely monitored for safety reasons. For the CC2 and HC3 cases the rotor rpm and wind tunnel speed had to be slightly reduced to keep the rotor shaft bending moment below the critical value.

The total rotor forces and moments are the summed result of the loads of the four blades. As such, the measured blade bending moment proved very useful for understanding the rotor loads. It was found that not only 1/rev but also 2/rev blade bending modes are important, especially for the CC1, HC3 and CC2 conditions and this explains why for these conditions

the rotor forces and moments do not only display large 4/ref but also 8/rev signal content. Subsequent analysis showed that the 2/rev blade bending mode is probably due to model vibration Eigen-modes, e.g. symmetric and anti-symmetric nacelle rotation around the quarter chord wing axis.

The present analysis shows the periodic nature of the rotor forces and moments under a variety of rotor inflow conditions. Focus was on the trimmed reference conditions. The presented results are well suited to validate or verify existing semi-empirical or CFD methods to predict such periodic effects.

Further exploitation of the data set is anticipated, e.g. correlation between unsteady wing pressures and flap loads with the rotor azimuthal position.

The measurements and data analysis was made in the framework of the EU co-funded 5th Framework project NICETRIP and involved contributions from partners Agusta-Westland, DLR, NLR and ONERA.

COPYRIGHT STATEMENT

The author(s) confirm that they, and/or their company or organization, hold copyright on all of the original material included in this paper. The authors also confirm that they have obtained permission, from the copyright holder of any third party material included in this paper, to publish it as part of their paper. The author(s) confirm that they give permission, or have obtained permission from the copyright holder of this paper, for the publication and distribution of this paper as part of the ERF2014 proceedings or as individual offprints from the proceedings and for inclusion in a freely accessible web-based repository.

Test case	Ref Dpt	Ma_tip -	rpm 1/min	Ma_wt -	vel m/s	Alpa_sti deg	delAlpha deg	AngNac deg	AngWing deg	AngElev deg
AC1	2192	0.4672	2100	0.170	59.2	10.04	0.00	0.0	0.0	-19.0
CC4	2311	0.6037	2730	0.168	59.2	5.19	0.15	30.0	4.2	-5.5
CC4, no cyclics	2835	0.6080	2730	0.169	59.1	5.27	0.15	30.0	4.2	-4.5
HC2	2363	0.6227	2765	0.059	20.2	-0.53	1.44	81.0	45.9	12.1
HC2, no cyclics	2414	0.6223	2750	0.059	20.1	-3.60	1.45	86.7	46.0	12.1
CC1, no cyclics	2479	0.6239	2765	0.088	30.3	4.08	0.63	77.9	30.4	-1.3
HC3, no cyclics	2558	0.5603	2490	0.104	36.0	-5.15	0.34	86.6	18.6	15.7
CC2, no cyclics	2750	0.5590	2495	0.142	49.3	2.39	0.19	61.8	6.7	0.5
CC2_EP, no cyclics	2697	0.5567	2490	0.142	49.3	2.43	0.19	61.8	6.7	0.5
HC1, no cyclics	2867	0.6295	2790	0.000	0.0	0.02	0.00	89.9	80.0	-2.5

Table 1: Trimmed conditions for the model configurations tested in DNW-LLF wind tunnel

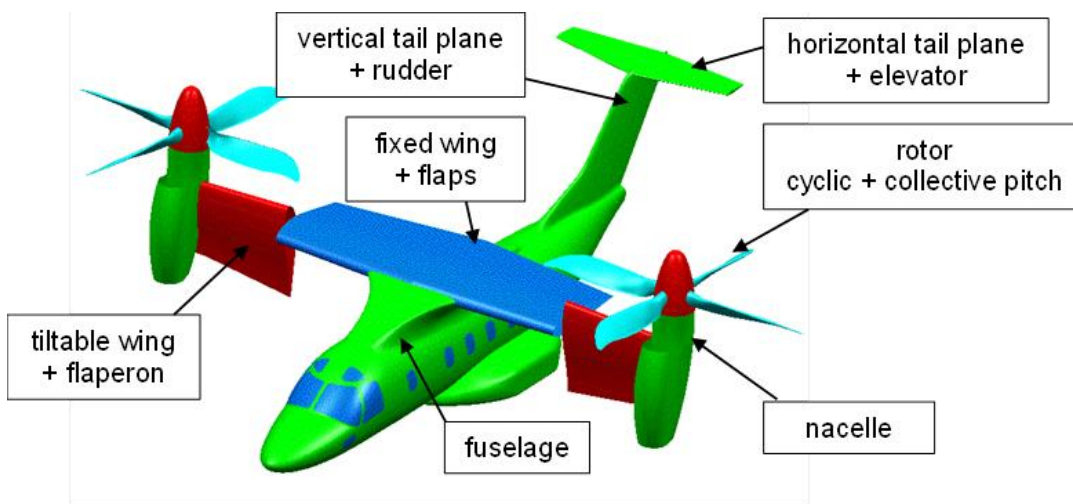


Figure 1: Sketch of ERICA configuration, showing the different model parts

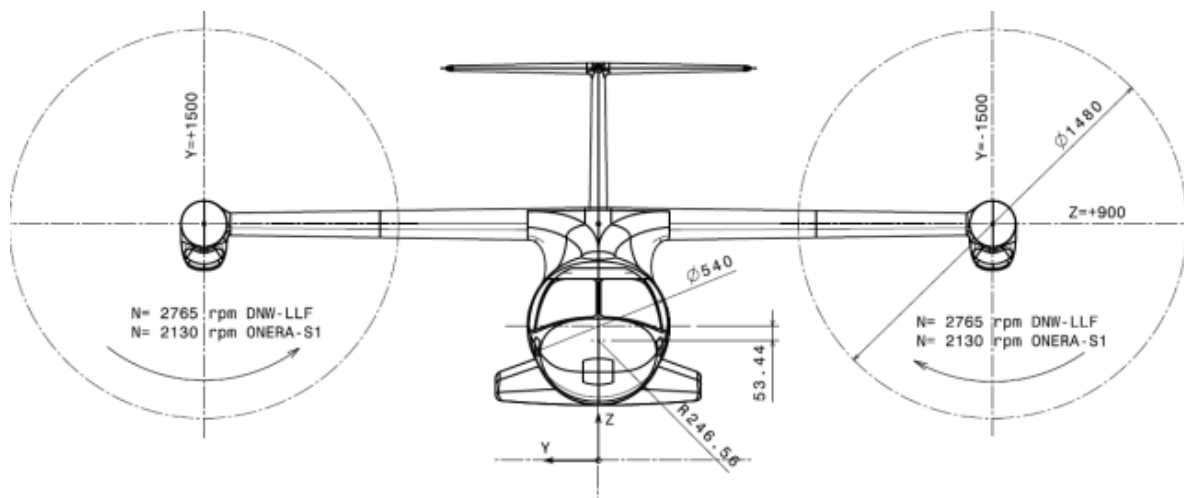


Figure 2: Front view and dimensions (in mm) of the ERICA wind tunnel model

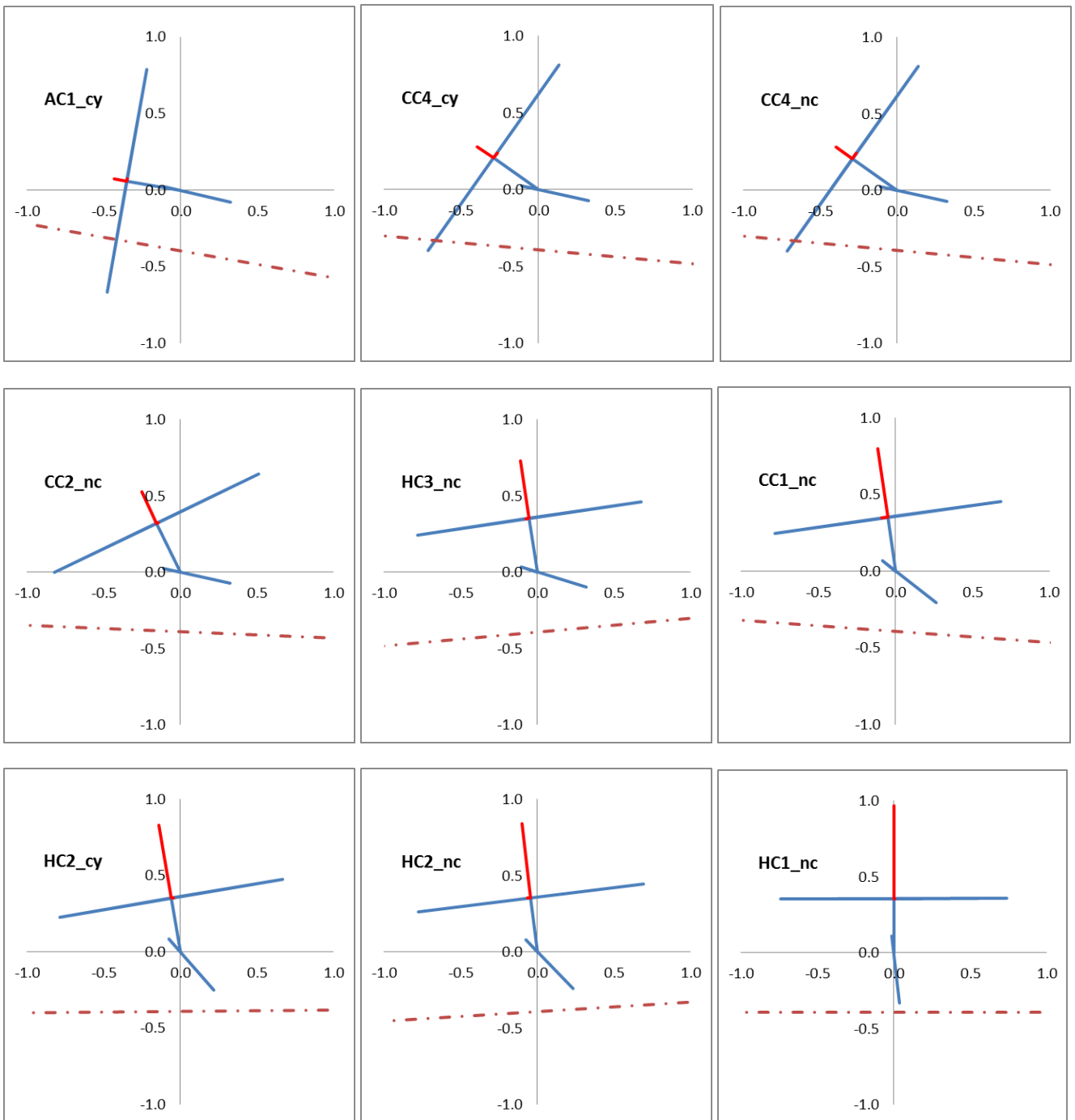


Figure 3: Sketch of rotor, rotor axis, wing tip chord and fuselage centerline (dashed) positions for the trimmed conditions. The average rotor thrust and in-plane Fz force are shown in red. The x-axis is parallel to the tunnel centerline, $(x,y)=(0,0)$ is the position of the nacelle rotation axis at the $\frac{1}{4}$ chord line

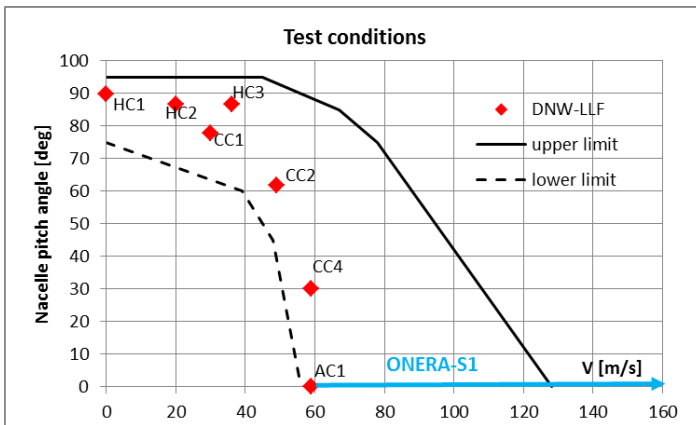


Figure 4: Test cases in DNW-LLF and ONERA-S1MA wind tunnel

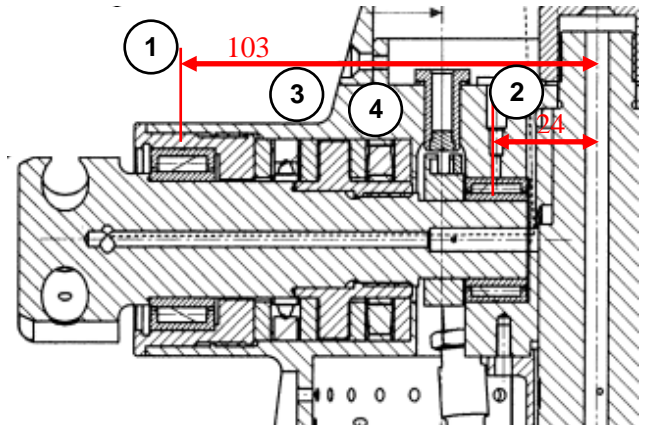


Figure 7: Blade shaft bearing positions #1 and #2 are radial needle type bearings and #3 and #4 are axial cylindrical roller bearings



Figure 5: Model on dorsal sting support in DNW-LLF



Figure 8: Broken blade axial bearing and damaged bearing ring due to high loads under cyclic blade movement

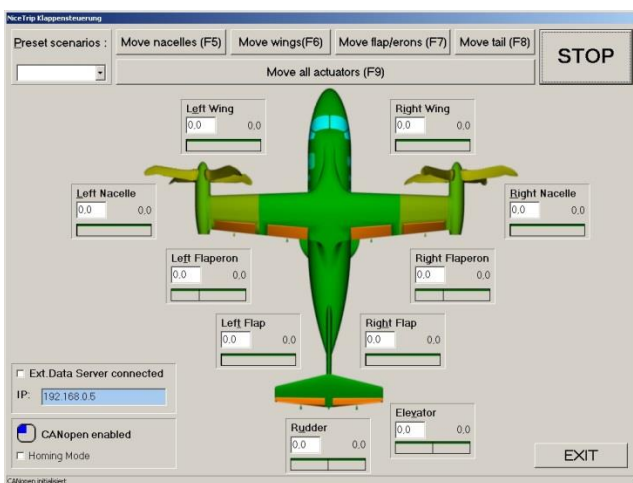


Figure 6: Actuator control interface (DLR)

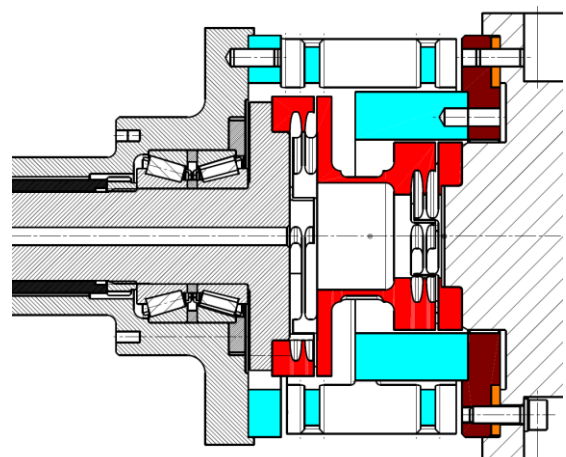


Figure 9: Rotor balance assembly

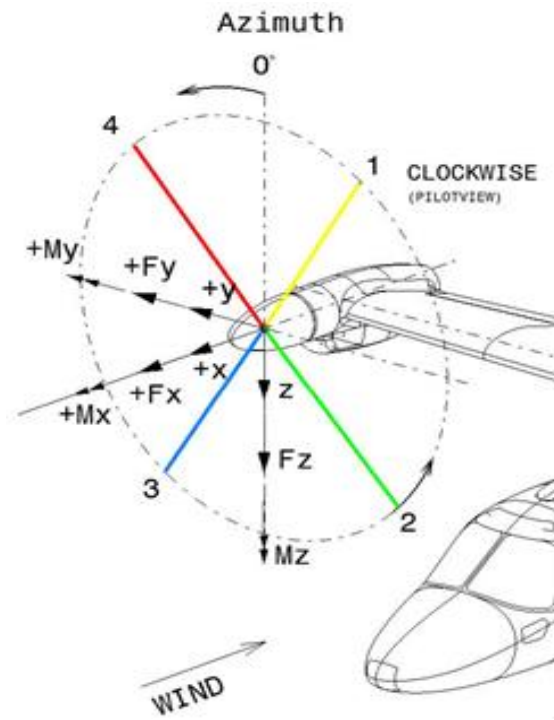
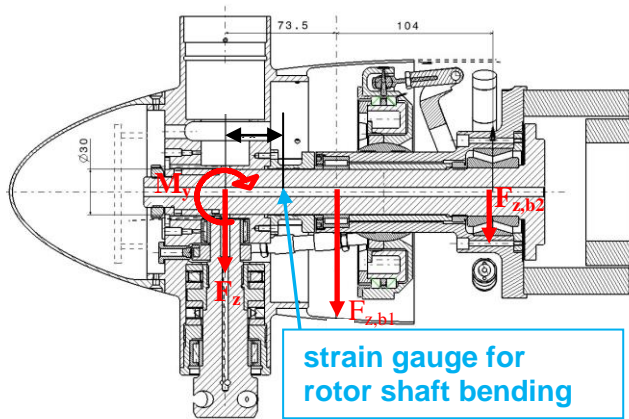
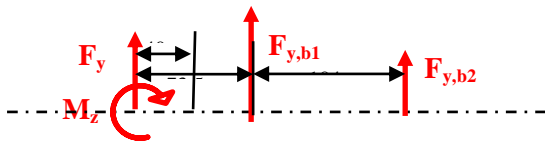


Figure 10: Definition of rotor axis system



a) in x-z plane



b) in x-y plane

Figure 11: Forces and moments on rotor shaft

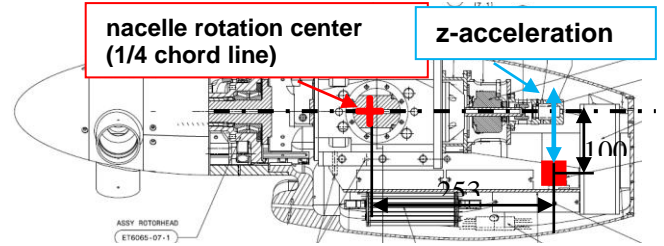


Figure 12: Position of accelerometer in nacelle

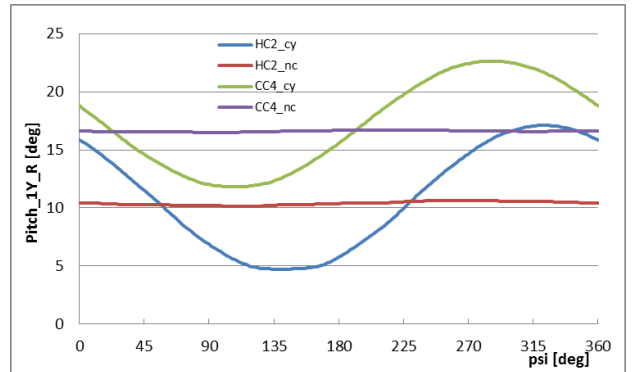


Figure 13: Blade pitch angle of RH rotor blade #1 as function of blade azimuth angle ψ

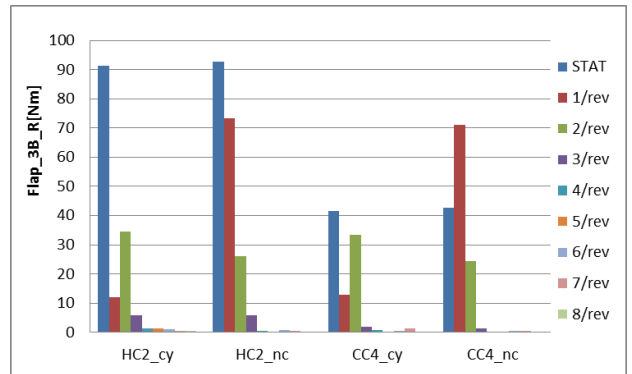


Figure 14: n/rev blade flap bending moment amplitudes, measured on RH rotor blade #3 [Nm]

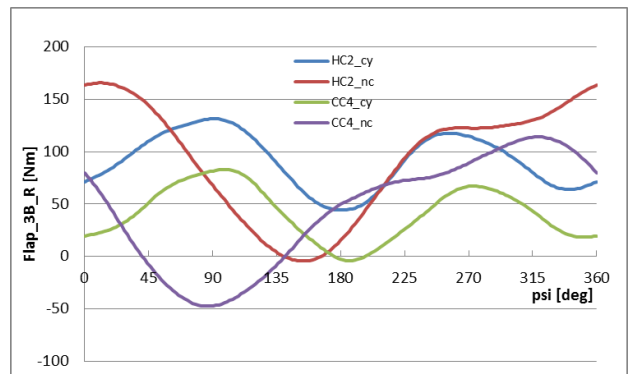


Figure 15: Blade flap bending moment of RH rotor blade #3 as function of blade #1 position angle

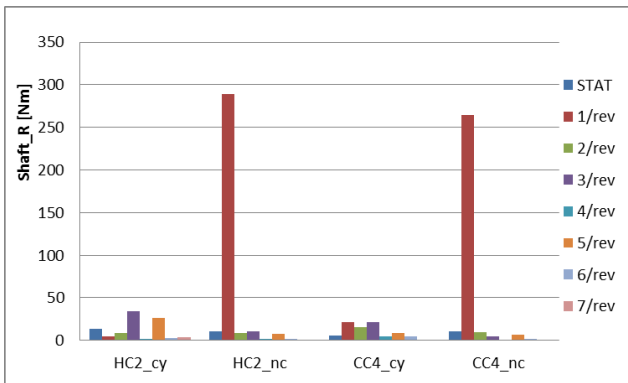


Figure 16: n/rev rotor shaft bending moment, measured by strain gauge sensor on RH rotor shaft

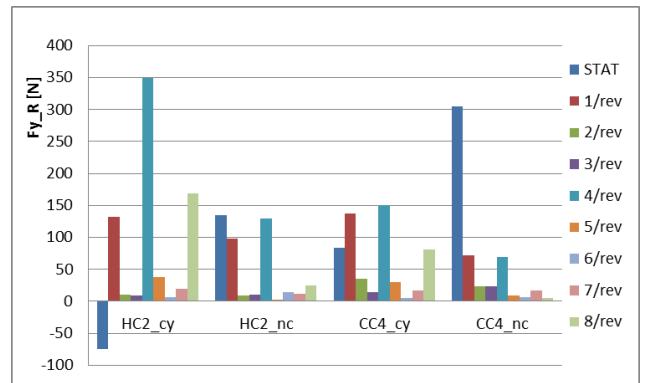


Figure 19: n/rev rotor in-plane force F_y [N], measured by RH rotor balance

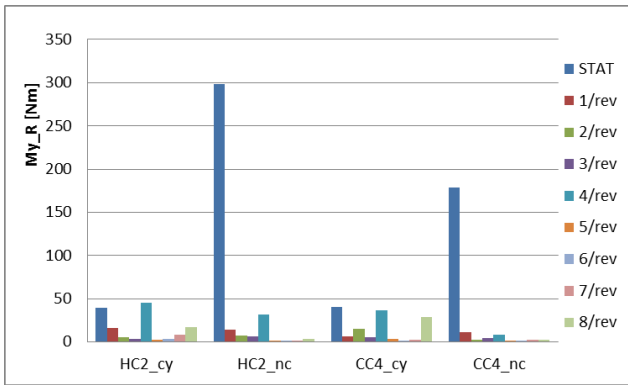


Figure 17: n/rev rotor in-plane moment M_y [Nm], measured by RH rotor balance

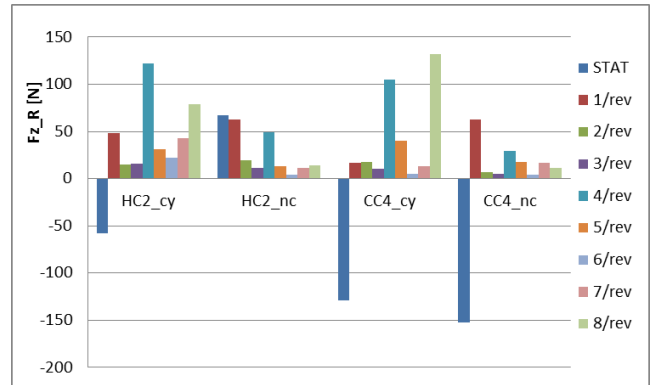


Figure 20: n/rev rotor in-plane force F_z [N], measured by RH rotor balance

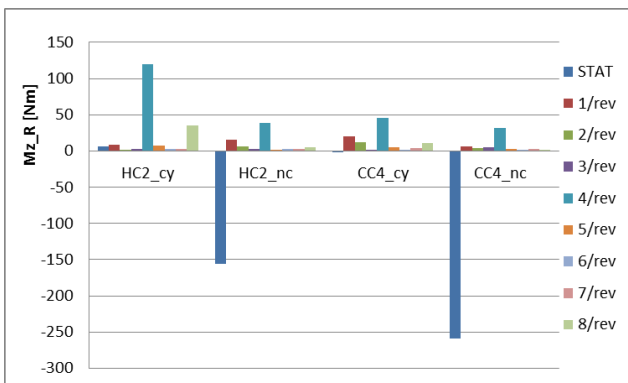


Figure 18: n/rev rotor in-plane moment M_z [Nm], measured by RH rotor balance

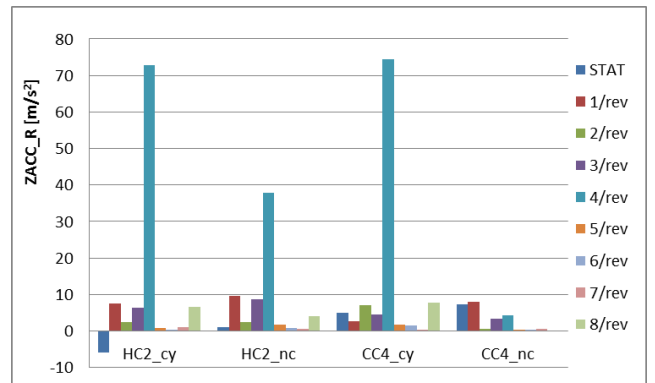


Figure 21: n/rev z-component of nacelle acceleration $[m/s^2]$, measured on RH nacelle (see figure 12)

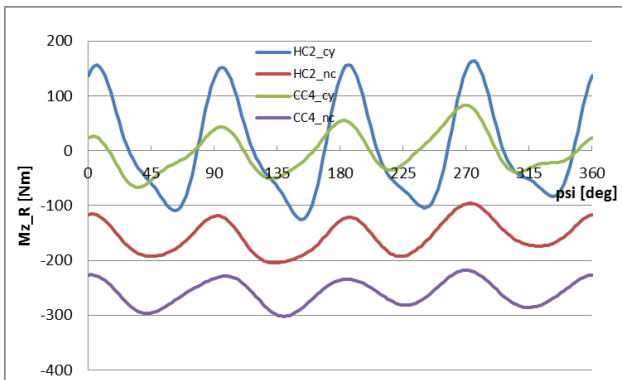


Figure 22: M_z as function of blade #1 position angle ψ , reconstructed from 1-8/rev signals measured with RH rotor balance

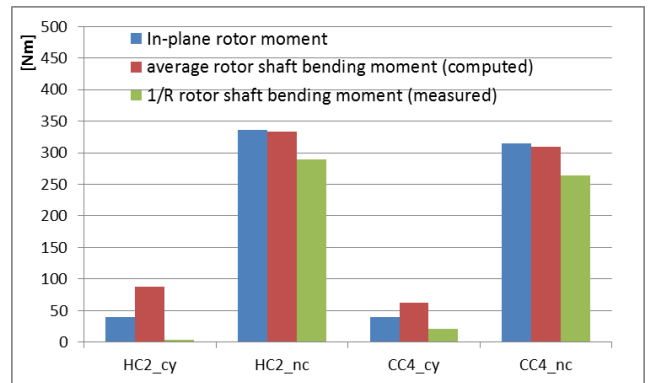


Figure 25: Measured total time-averaged in-plane moment, computed time-averaged rotor shaft bending moment at rotor shaft strain gauge position and measured 1/rev rotor shaft bending moment

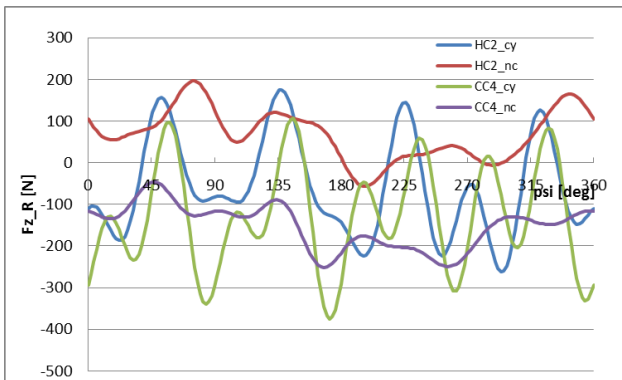


Figure 23: F_z as function of blade #1 position angle ψ , reconstructed from 1-8/rev signals measured with RH rotor balance

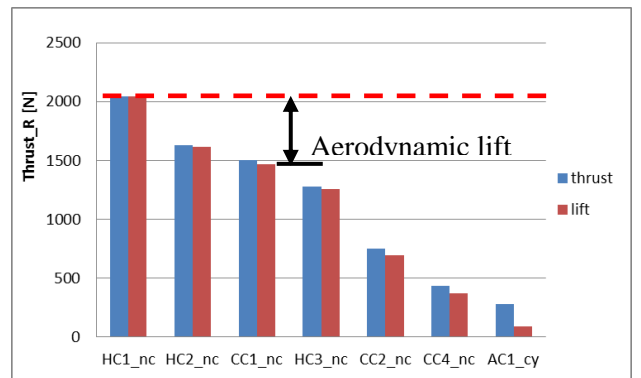


Figure 26: Rotor thrust and combined effect of measured rotor thrust and F_z on lift (for RH rotor balance)

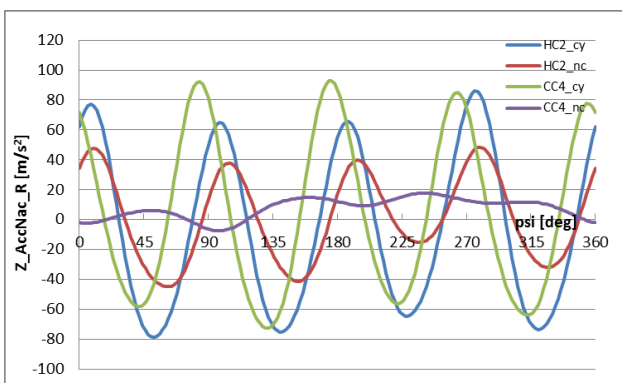


Figure 24: z component of RH nacelle acceleration $[m/s^2]$ as function of blade #1 position angle ψ , reconstructed from 1-8/rev signals

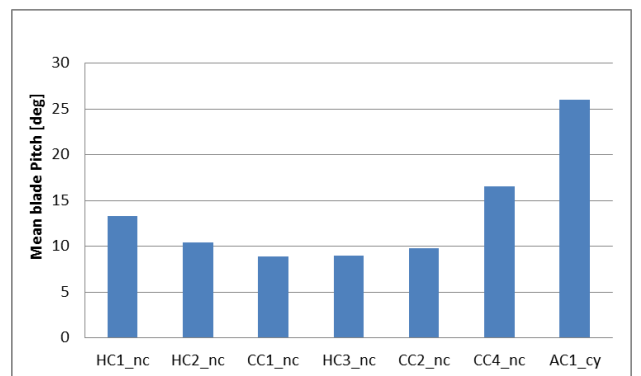


Figure 27: Blade pitch angle in trimmed conditions

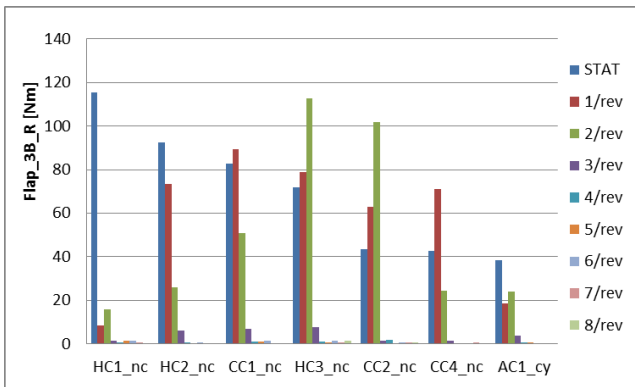


Figure 28: n/rev blade bending moment [Nm] measured with strain gauge at r/R=0.25 on RH blade #3

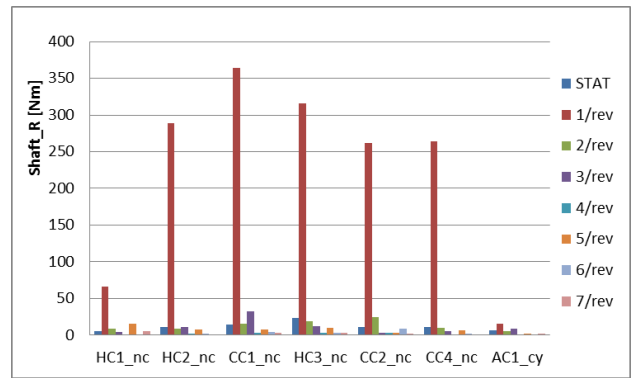


Figure 31: n/rev rotor shaft bending moment [Nm], measured with strain gauge at RH rotor shaft (see figure 11)

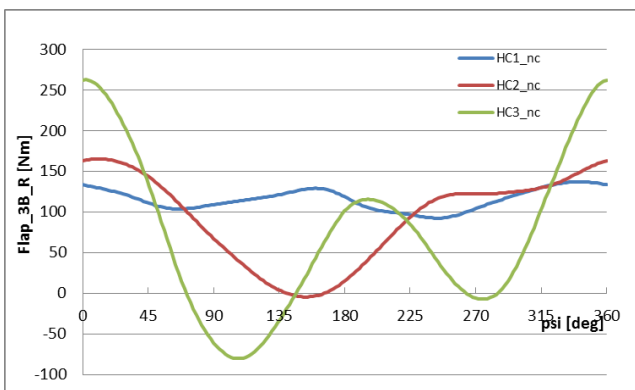


Figure 29: Blade bending moment [Nm] at r/R=0.25 of RH blade #3 as function of blade #1 position angle ψ , HC conditions

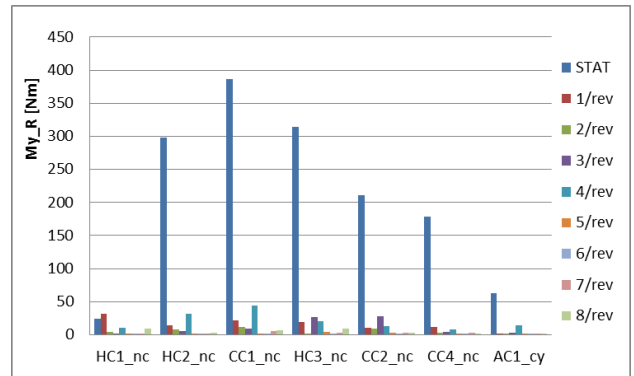


Figure 32: n/rev rotor in-plane moment M_y [Nm], measured with RH rotor balance

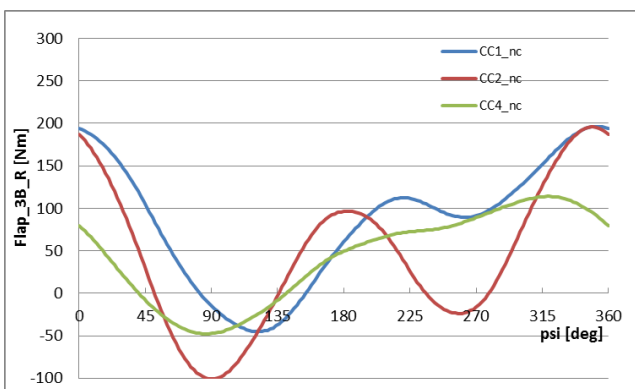


Figure 30: n/rev blade bending moment [Nm] at r/R=0.25 of RH blade #3 as function of blade #1 position angle ψ , CC conditions

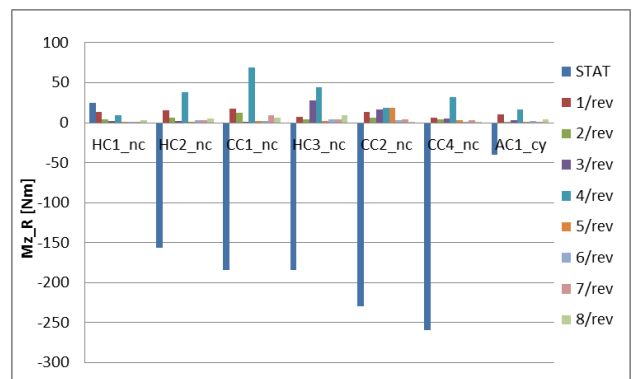


Figure 33: n/rev rotor in-plane moment M_z [Nm], measured with RH rotor balance

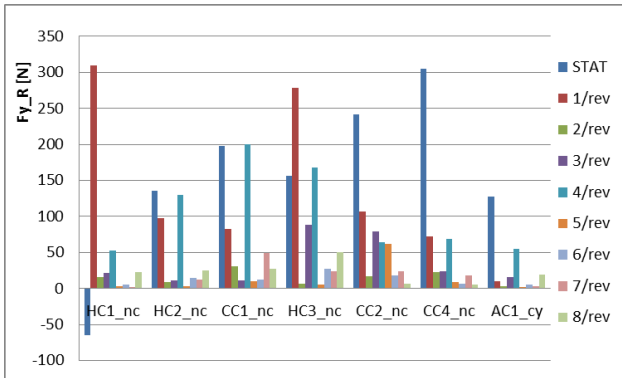


Figure 34: n/rev rotor in-plane force F_y [N], measured with RH rotor balance

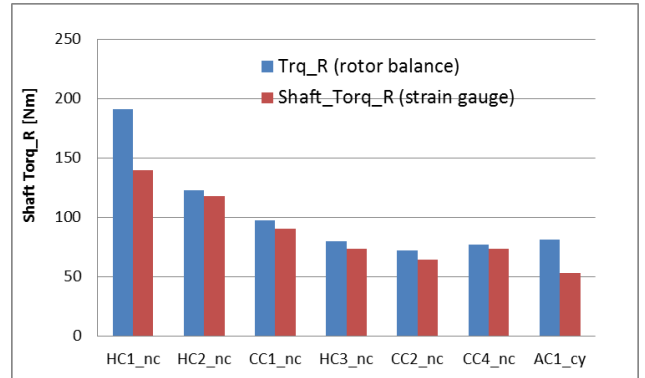


Figure 37: Comparison between RH rotor shaft torque from rotor balance and from rotor shaft strain gauge

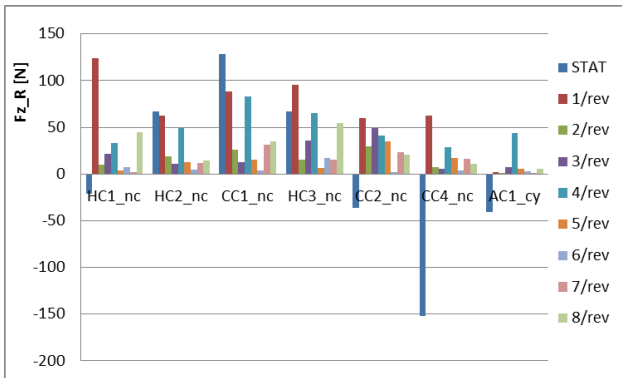


Figure 35: n/rev rotor in-plane force F_z [N], measured with RH rotor balance

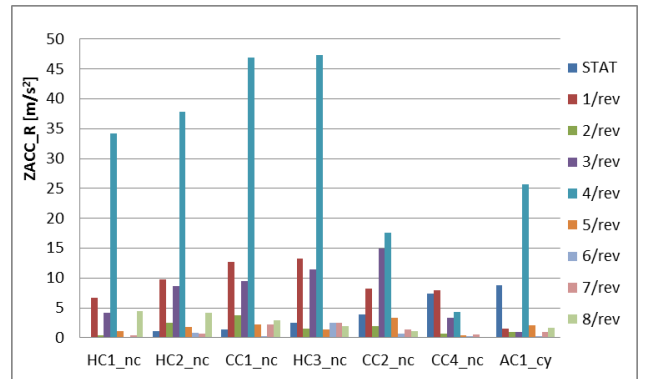


Figure 38: n/rev z-component of nacelle acceleration [m/s²], measured on RH nacelle (see figure 12)

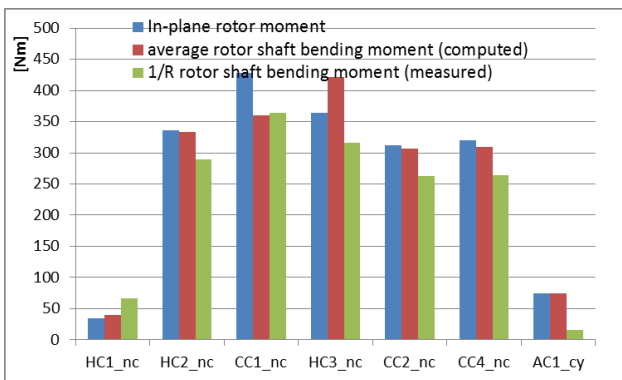


Figure 36: Measured total time-averaged in-plane moment, computed rotor shaft bending moment and measured 1/rev rotor shaft bending (RH rotor)

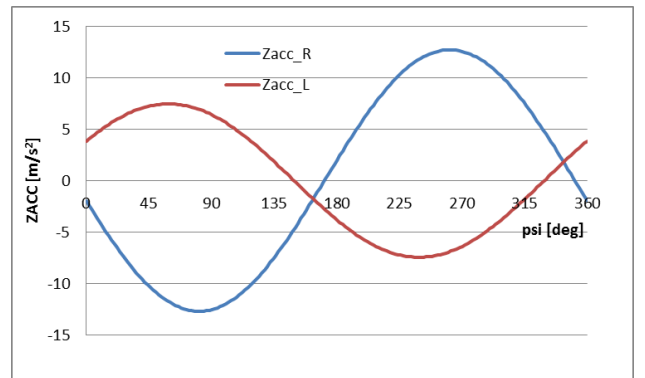


Figure 39: 1/rev z-component of nacelle acceleration [m/s²], measured for LH (top) and RH (bottom) nacelle

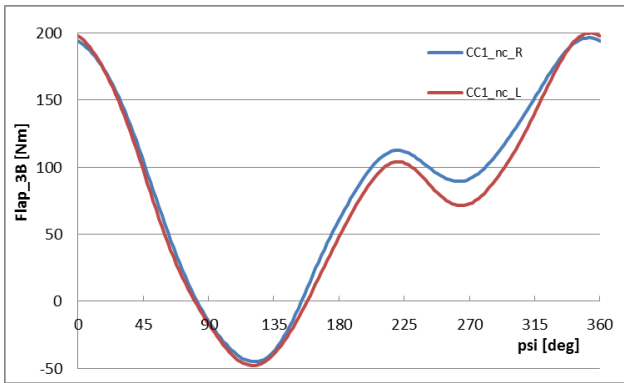


Figure 40: Blade bending moment [Nm] at $r/R=0.25$ of RH and LH blades #3 as function of blade RH blade #1 position angle ψ , CC1 condition

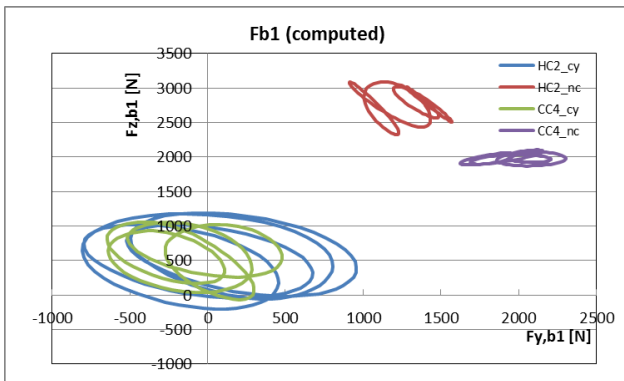


Figure 41: Computed forces on rotor shaft bearing #1 (see figure 11) during one blade revolution, for HC2 and CC4 configuration with and without cyclic pitch

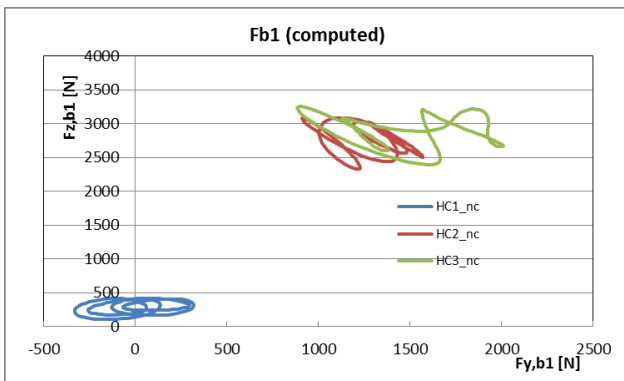


Figure 42: Computed forces on rotor shaft bearing #1 (see figure 11) during one blade revolution, for HC1, HC2 and HC3 without cyclic pitch